Preprints.org

Article

Facile Hydrothermal Synthesis of Ag/Fe$_3$O$_4$/Cellulose Nanocrystals Nanocomposite as Highly Active Catalyst for 4-Nitrophenol and Toxic Organic Dyes

An Nang Vu , Hoa Ngoc Thi Le , Thang Bach Phan , Hieu Van Le [*]

Article

Facile Hydrothermal Synthesis of Ag/Fe₃O₄/Cellulose Nanocrystals Nanocomposite as Highly Active Catalyst for 4-Nitrophenol and Toxic Organic Dyes

Vu Nang An [1,2,†], Le Thi Ngoc Hoa [1,2,3,†], Phan Bach Thang [2,4] and Le Van Hieu [1,2,3,*]

[1] Faculty of Materials Science and Technology, University of Science, VNU–HCM, Ho Chi Minh City 700000, Viet Nam; vnan@hcmus.edu.vn (V.N.A.); ltnhoa@hcmus.edu.vn (L.T.N.H.)

[2] Vietnam National University Ho Chi Minh City, Ho Chi Minh City 700000, Vietnam; pbthang@inomar.edu.vn

[3] Laboratory of Multifunctional Materials, University of Science, VNU–HCM, Ho Chi Minh City 700000, Vietnam

[4] Center for Innovative Materials and Architectures, VNU-HCM, Ho Chi Minh City 700000, Vietnam

[*] Corresponding: lvhieu@hcmus.edu.vn

[†] These authors contributed equally to this work.

Abstract: Novel effluent treatment solutions for dangerous organic pollutants are crucial worldwide. In recent years, chemical reduction using noble metal-based nanocatalysts and $NaBH_4$, a reducing agent, has become common practice for eliminating organic contaminants from aquatic environments. We suggest a straightforward approach to synthesizing magnetic cellulose nanocrystals (CNC) modified with magnetite (Fe_3O_4) and silver nanoparticles (Ag NPs) as a catalyst for organic contamination removal. Especially, Ag NPs were decorated on the CNC surface without reducing agents or stabilizers by reducing $AgNO_3$. XRD, FE-SEM, TEM, EDX, VSM, BET, and zeta potential tests characterized the Ag/Fe_3O_4/CNC nanocomposite. The nanocomposite's catalytic activity was tested by eliminating 4-nitrophenol (4-NP) and organic dyes methylene blue (MB) and methyl orange (MO) in an aqueous solution at 25 °C. The Ag/Fe_3O_4/CNC nanocomposite reduced 4-NP and decolored these hazardous organic dyes in short time (2 to 5 min) using a tiny amount of catalyst (2.5 mg for 4-NP and 15 mg for MO and MB). The magnetic catalyst was removed and reused three times without losing catalytic activity. This work shows that the Ag/Fe_3O_4/CNC nanocomposite can chemically reduce harmful pollutants in effluent for environmental applications.

Keywords: catalytic dye reduction; cellulose nanocrystals; magnetic nanocomposite; 4-nitrophenol; wastewater treatment

1. Introduction

Environmental pollution has become a global and grave threat to human health despite the exponential development of modern industries over the past few decades. In recent years, the contamination of water bodies by releasing untreated water containing inorganic and organic species has garnered significant attention among the various types of environmental pollution [1–3]. Notably, it is believed that the uncontrolled discharge of azo dyes, widely used in the leather, fabric, plastic, personal care products, ink, paper, and food industries, causes significant damage to aquatic ecosystems [4,5]. Due to their photo-, thermal-, and biodegradation-resistance, organic dyes can endure for an extended period in the environment. The existence and stability of these oxygen-sequestering species in water systems have been reported to diminish light penetration and hinder photosynthesis in aquatic vegetation [6]. Before they can be discharged safely into the natural environment, industrial effluents carrying harmful organic dyes must be degraded and decolored.

In addition to organic azo pigments, the United States Environmental Protection Agency (U.S. EPA) considers phenolic compounds, such as the well-known nitrophenol derivatives, to be priority pollutants that directly affect the environment and human health [7]. Known refractory 4-nitrophenol (4-NP) sources in water bodies include petrochemical, pesticide, pharmaceutical, preservative,

explosive, pigment, and wood industries [8,9]. Before releasing them into the environment, developing efficient techniques for extracting them from industrial effluent is critical. The catalytic conversion of 4-NP to its amino counterpart, 4-aminophenol (4-AP), has generated significant interest in environmental cleanup. The essential roles amino acids perform in pharmaceutical and photographic applications are well-known [10]. 4-AP is a critical intermediate in synthesizing numerous antipyretic and analgesic pharmaceuticals, while its strong reducing properties are utilized in photographic development. Therefore, developing high-performance materials for pigment degradation and 4-NP reduction can significantly reduce environmental pollution. In recent years, nano-sized metals with controlled morphology and texture have been favored over their bulk counterparts because of their enhanced catalytic, magnetic, electronic, and optical properties [11–13]. Notably, noble metal nanoparticles exhibit dense packing, unconstrained electrons in the valence band, and a high surface-to-volume ratio [14]. Due to their desirable physical and chemical properties [15,16], using inexpensive silver nanoparticles (Ag NPs) in catalysis, sensors, cosmetics, and disinfecting medical devices is becoming increasingly investigated. Controlled growth, particle size, morphology, and long-term stability play significant roles in the performance activity of Ag NPs.

Nevertheless, metal nanoparticles with desirable morphological properties as catalysts have disadvantages such as (i) a tendency to aggregate, resulting in decreased efficiency due to their more incredible surface energy, and (ii) difficult recovery from the medium of reaction for reuse due to their nanoscale size   [17,18]. Innovative techniques for immobilizing metal nanoparticles on solid supports to generate hybrid nanostructures have been developed to address these drawbacks. Interestingly, the direct immobilization of Ag NPs on other active materials, such as Fe_3O_4, makes them ideally suited for use as a catalyst; unfortunately, the repulsive forces between them must be surmounted to ensure their stability. Introducing a buffer (organic) layer between the two active materials can alleviate the issue of repulsive forces and bring about strong synergy in the hybrid structure for efficient catalytic activity [19–22].

In recent years, biomass has attracted concern regarding the design of nanostructure catalysts based on a porous structure and numerous active sites for fixing metal nanoparticles [23–26]. Specifically, cellulose is the most overall biomass extensively studied to produce stable metal nanoparticles [27–31]. Li et al. created substrates for synthesizing Ag-Fe_3O_4 nanoparticles by functionalizing polydopamine-containing porous cellulose acetate microspheres [27]. In synthesized cellulose microcrystals, Fe-Cu alloy nanocatalyst is immobilized. These materials are combined with $NaBH_4$ to convert nitroaren to arylamine in water. The reaction occurs within 5 to 14 min and is highly effective [32]. Moreover, cellulose can be transformed into various polymorphs using an environmentally friendly mixture of NaOH and Urea [33–35], and through hydrolysis, cellulose nanocrystals (CNC) with high physical properties can be obtained.

In this research, a simple and environmentally friendly hydrothermal method for preparing Ag/Fe_3O_4/CNC nanocomposite was developed. The Ag/Fe_3O_4/CNC nanocomposite's phase structure, morphology, magnetic property, and thermal stability were investigated in detail. In addition, catalytic reduction experiments were conducted, and the results demonstrated that the as-prepared Ag/Fe_3O_4/CNC nanocomposites had a high catalytic performance for the reduction of 4-NP, MO, and MB in the presence of sodium borohydride ($NaBH_4$) as an electron donor. Compared to previous works, the current work possesses many advantages. First, neutral deionized water was used as the system's solvent. Second, the green and inexpensive synthetic route requires no chemical-reducing agents. In addition, CNC was produced by acid-hydrolysis cellulose, which was isolated from by-product fibers of coconut husk. It is one of the most effective methods for creating economic materials from agricultural by-products, which are nearly abundant in Vietnam.

2. Materials and Methods

2.1. Materials

Coconut husk fiber was collected from Mo Cay Nam district, Ben Tre province. After harvesting, coconut products were separated from outside shells, and then they were crushed, dried, removed softened fiber from coconut shells, and split into coconut fiber. Coconut fiber is 10-20 cm long,

yellowish-brown in color, and twisted together, which was crushed into powder. Formic acid (HCOOH, 90%), hydroperoxide (H_2O_2, 30%), sodium hydroxide (NaOH, 96%), hydrochloric acid (HCl, 37%), urea ((NH_2)$_2$CO, ≥ 99%), ethylene glycol (HOCH$_2$CH$_2$OH, ≥ 99%), ethanol (C_2H_5OH, 99,5%), and two precursors of Fe and Ag are iron(III) chloride hexahydrate ($FeCl_3.6H_2O$, 97%) silver nitrate ($AgNO_3$, 99%) were purchased from XiLong, China. MO ($C_{14}H_{14}N_3NaO_3S$, ≥ 95%), MB ($C_{16}H_{18}N_3SCl$, ≥ 95%), sodium borohydride ($NaBH_4$, ≥ 99%), and 4-NP (≥ 99%) were purchased from Sigma-Aldrich. All chemicals and reagents were used as received without further purification.

2.2. Isolation of Cellulose from Coconut Fiber and Hydrolysis to Generate CNC

The isolation of cellulose from coconut fiber using the formic acid/peroxyformic acid process was conducted as in our previous work [36]. There are three majority steps to isolate cellulose: treatment with formic acid (HCOOH), treatment with peroxyformic acid (PFA-HCOOH + H_2O_2 + H_2O mixture), and bleach with NaOH and H_2O_2 solution. Firstly, coconut fiber powder was stirred with distilled water at 90 °C for 2 hours following a ratio of 1:20 (coconut fiber weight: volume of water). Next, the sample was filtered, washed in distilled water, and dried at 60 °C. Then, coconut fiber was stirred with a reflux condenser in acid HCOOH 90% under the coconut fiber weight: HCOOH volume of 1:10 at 90 °C for 2 hours. After HCOOH treatment, the mixture was filtered and washed with distilled water to remove excess acid. The sample was dried at 60 °C. Coconut fiber was continuously treated with a PFA mixture (90% HCOOH 90%, 4% H_2O_2 30%, and 6% distilled water) under a 1:20 ratio (fiber weight: PFA volume). The system was mechanically stirred with reflux at 100 °C for 2 hours. Finally, fiber was bleached to obtain pure cellulose. Specifically, 6.0 g of PFA-treated fiber was put into a three-neck round bottom flask 500 mL, and then a solution of 180 mL distilled water and 12 mL NaOH was added into the flask, and the system was heated to 70 °C. After that, 16 mL H_2O_2 30% was slowly poured into the system and started to set time in 1 hour (all H_2O_2 was poured within 15 min). The system was kept in stable heat at 80 °C. The mixture was then filtered and washed in distilled water. The sample obtained is cellulose, which was dried at 80 °C.

The cellulose was hydrolyzed with hydrochloric acid HCl 6M under a 1:25 (cellulose weight/ HCl volume) ratio. The system was stirred at a stable temperature of 90 °C for 3 hours. When the reaction finished, the mixture was put into a beaker that contained 1000 mL distilled water and obtained suspension. The suspension was deposited, changed the water a few times, centrifuged with a rate of 6000 rpm for 10 min, then dried at 80 °C. The final sample obtained is CNC.

2.3. Preparation of Fe$_3$O$_4$ Nanoparticles by Solvothermal Method

The manufacture of Fe_3O_4 nanoparticles using the solvothermal technique is depicted in Figure 1. First, 42.0 mL of ethylene glycol and 1.5 mL of distilled water were combined with 0.43 g $FeCl_3.6H_2O$ and 0.90 g (NH_2)$_2$CO to generate an orange solution. This mixture was then ultrasonically processed for 30 min. The combined solution was then put into a Teflon-lined stainless steel autoclave, sealed for six hours, and heated to 220 °C before being cooled to ambient temperature. After obtaining black precipitation of Fe_3O_4, the sample was centrifuged five to six times with ethanol. The Fe_3O_4 nanoparticles were made after washing and vacuum drying at 60 °C for 9 hours.
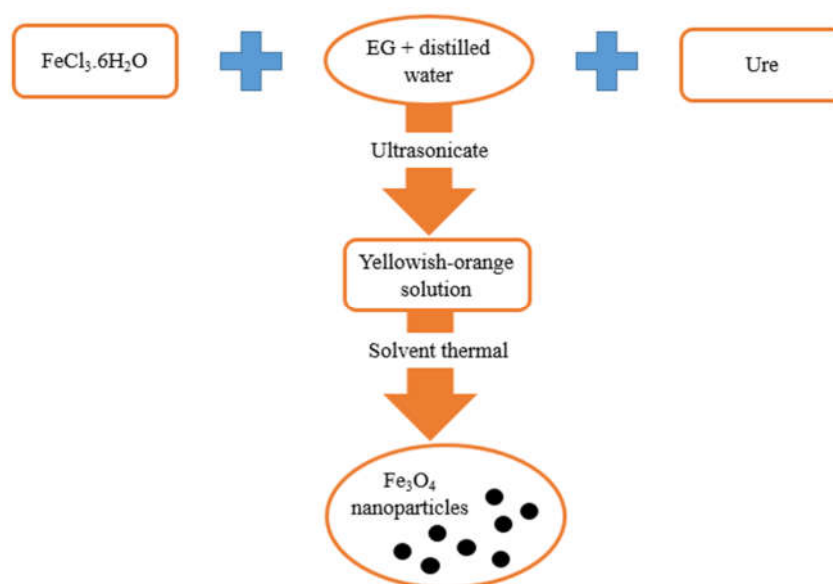
Figure 1. The synthesis process of Fe_3O_4 nanoparticles**.**

2.4. Preparation of Ag/Fe$_3$O$_4$/CNC Nanocomposite by Hydrothermal Method

The experimental procedure involved subjecting a mixture comprising 10 mL of CNC (10 mg. mL^{-1}), 10 mL of Fe_3O_4 (2 mg. mL^{-1}), and 10 mL of $AgNO_3$ (17 mg. mL^{-1}) to ultrasonic treatment for 30 min. Subsequently, the mixture was transferred into a Teflon-lined stainless steel autoclave and subjected to hydrothermal treatment at a temperature of 80 °C for a period of 3, 4, and 5 hours. When the hydrothermal process finished, a suspension of Ag/Fe$_3$O$_4$/CNC nanocomposite was obtained, then centrifuged and washed with DI water several times and ethanol three times before drying at 70 °C for 3 hours. The obtained products were labeled FAC3, FAC4, and FAC5, corresponding to the hydrothermal times. In addition, for comparative purposes, Ag/Fe$_3$O$_4$ (FA) samples were synthesized without CNC at three separate times: 3 hours, 4 hours, and 5 hours under the same conditions.

2.5. Characterization

The crystal structure was characterized by X-ray diffraction (XRD), which was implemented on a Bruker D2 Phaser XRD (Germany) instrument with Cu *Kα* (target) radiation ($\lambda = 1.5418$ Å) at a scan rate (2θ) of 0.02^0 min^{-1} and a scan range of 10^0 to 80^0. The samples were ground into a fine powder and placed into a groove on a glass slide. After being compacted, the slide with the powder was used for XRD experiments. Morphology was characterized by field emission scanning electron microscopy (FESEM, Hitachi S4800) equipped with an energy-dispersive X-ray (EDX) spectrometer for elemental analysis. A sample patch was adhered to a specimen stage by conductive adhesive tapes. Before the observation, the sample was sputtered with gold for electrical conduction. Transmission electron microscopy (TEM) was performed with a   JEM-1400 F (JEOL Ltd., Japan) with a field emission gun operating at 100 kV. The sample was suspended in ethanol and was prepared by being drop-cast onto a carbon-coated 200-mesh copper grid and subsequently dried at room temperature. The magnetic properties of the obtained materials were measured with a vibrating sample magnetometer (VSM, LakeShore 7073, USA) at 25 °C, and the hysteresis loop was measured in a magnetic field from—12000 to +12000 Oe. Thermogravimetric (TG) analysis was performed with a synchronous thermal analyzer (SDTQ600, USA) under a nitrogen atmosphere from room temperature to 800 °C at a heating rate of 10 °C. min^{-1}.

The specific surface areas of the FA5 and FAC5 were measured using a Quantachrome Nova 2200 (USA) BET analyzer and the Brunauer-Emmett-Teller (BET) method based on low-temperature N_2 adsorption-desorption. The Barrett-Joyner-Halanda (BJH) method was used to calculate the pore size distributions from the adsorption isotherms. The diluted FAC5 suspension

was sonicated before DLS analysis. The material was placed in the cuvette to be measured by a zeta analyzer (Nano ZS90, Malvern Zeta sizer, United Kingdom).

2.6. Catalytic Study

2.6.1. Catalytic Reduction of 4-NP

The conversion of 4-NP to 4-AP served as a model for evaluating the catalytic activity of the FAC5 nanocomposite. In a typical process, 2.5 mg of FAC5 catalyst was added to a 25 mL aqueous 4-NP (1×10^{-4} M) while the solution was agitated at 25 °C. Next, a 2.5 mL aqueous solution of NaBH$_4$ (1×10^{-4} M) was slowly added to the previously described reaction mixture. A sudden change from light yellow to a deeper yellow was observed. Changes in absorbance at 400 nm for 4-NP and 300 nm for newly created 4-AP were used to monitor the progression of the -NO$_2$ conversion at predetermined intervals. Within 10 min of reaction time, the pigment changed from rich yellow to colorless.

2.6.2. Catalytic Reduction of MO and MB Dyes

In this study, MO and MB were chosen as models for reduction and degradation by FAC5 in the presence of NaBH$_4$. In a typical decomposition procedure, 15 mg of FAC5 was added to 30 mL of an aqueous dye solution with a concentration of 1×10^{-4} M. The reaction was stirred at 25 °C while adding 1 mL of freshly prepared NaBH$_4$ solution (1×10^{-1} M). The supernatant's catalytic activity was determined using UV–vis absorption spectra (λ_{max}: 464 nm for MO; λ_{max}: 662 nm for MB) at predetermined time intervals.

3. Results and Discussion

3.1. Characterization

The XRD patterns depicted the crystal structure of the Fe$_3$O$_4$ and Fe$_3$O$_4$/Ag NPs in Figure 2a. The diffraction peaks at 2θ values of 30.1, 35.5, 43.1, 56.9, and 62.6°, which were assigned to the (220), (311), (400), (511), and (440) planes of the face-centered cubic structure of Fe$_3$O$_4$ (JCPDS card no. 79-0418), confirm the synthesis of Fe$_3$O$_4$ NPs [37,38]. While the peaks of Fe$_3$O$_4$/Ag NPs prepared at three different hydrothermal times can be observed at 38.2, 44.6, 64.5°, and 77.5 ° corresponding to the reflections of (111), (200), (220), and (311) crystal planes of Ag (JCPDS card no. 87-0720), indicating the face-centered cubic structure of the Ag NPs [39].
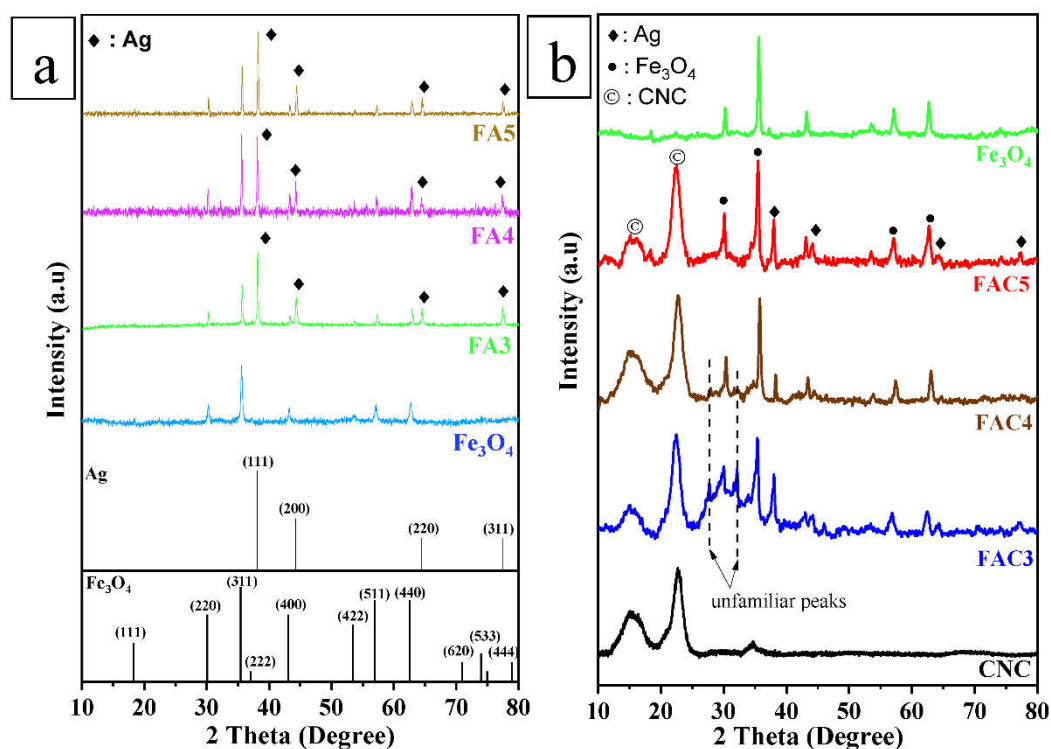
Figure 2. The XRD patterns of (a) Fe_3O_4 and FA materials synthesized at three different hydrothermal times, and (b) CNC and FAC materials synthesized at three different hydrothermal times.

Figure 2b depicts the XRD patterns of CNC, Fe_3O_4, and three FAC materials synthesized at three different hydrothermal times. Comparing the XRD patterns of the three FAC samples reveals that the characteristic Fe_3O_4 and CNC diffraction peaks at the 2θ positions are nearly unchanged. However, in the XRD diffractograms of FAC3 and FAC4, the intensity of the remaining characteristic peaks is comparatively low, except the silver (111) lattice peak at $2\theta = 38.2°$. In addition, there are impressive peaks at positions $2\theta = 27.7°$ and $32.1°$; the intensity of these peaks diminished gradually from the 3 hours hydrothermal sample to the 4 hours hydrothermal sample and disappeared by the 5 hours hydrothermal sample. More time may have been required for CNC to convert Ag^+ ions to Ag, resulting in the appearance of these unfamiliar peaks. The reduction reaction had yet to occur fully. When the reaction time is increased to 5 hours, the CNC has sufficient time to convert all Ag^+ ions to Ag, resulting in the disappearance of these peaks and an increase in the intensity of the diffraction peaks that characterize the Ag crystal structure.

The FE-SEM image of Fe_3O_4 (Figure 3a) reveals that the solvothermal-fabricated Fe_3O_4 has a spherical shape with an average diameter of approximately 300 nm. Figure 3b depicts the EDX spectrum of Fe_3O_4, which confirms this material has high purity when only Fe and O elements are present, with no other impurities. At three different time intervals, the hydrothermal treatment of Fe_3O_4 in $AgNO_3$ solution produced FA materials with remarkably similar morphology. In contrast to Fe_3O_4, the formation and attachment of Ag to the surface of Fe_3O_4 during the hydrothermal process gives FA spherical particles an uneven surface (Figure 4). The FAC material indicates that Fe_3O_4, Ag, or Ag/ Fe_3O_4 particles form on the CNC surface in the presence of the CNC. The FE-SEM imaging results indicate that the average particle size in the hydrothermal sample after 3 hours is approximately 180 nm; after 4 hours, it is approximately 150 nm; and after 5 hours, it is approximately 70-100 nm (Figure 4). When hydrothermal durations are between 3 and 4 hours, nanoparticles are unevenly distributed and tend to clump together. When the hydrothermal time is sufficiently extended (5 hours), the particle density becomes more remarkable than that of the two preceding samples. The 5-hour nanoparticles disperse uniformly on the surface of crystalline cellulose and are

less susceptible to agglomeration. As the hydrothermal duration increases, the particle density on the CNC surface increases, the particle size decreases, and the particles disperse more effectively.
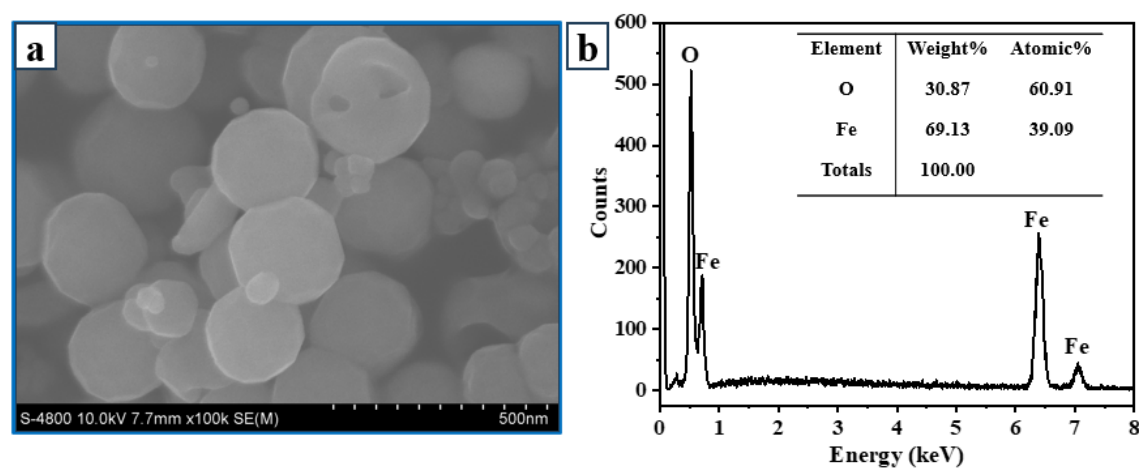

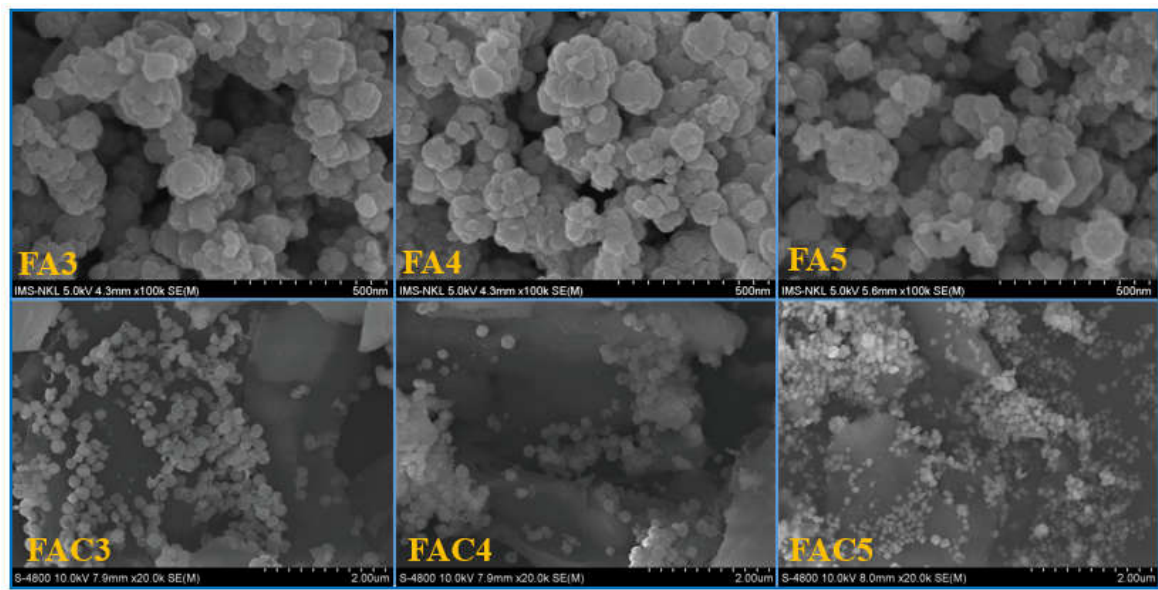**Figure 3.** FE-SEM image (a) and EDX spectrum (b) of Fe_3O_4 NPs.

Figure 4. FE-SEM images of FA and FAC materials.

The results of the TEM image analysis (shown in Figure 5) make the composition of the FAC composites quite evident. The Ag NPs and the Fe_3O_4 NPs are interconnected and dispersed across the surface of the CNC bearing. The amount of time spent in the hydrothermal process causes the particle size of the Fe_3O_4 to decrease gradually. Additionally, the particles become more densely packed and uniformly distributed.
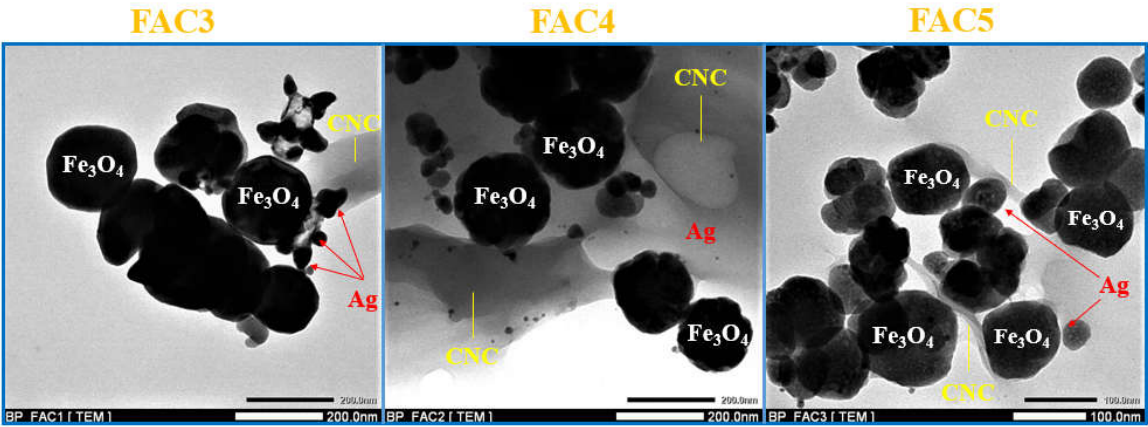
Figure 5. TEM images of FAC materials**.**

Figure 6 shows the EDX spectrum of samples FA5 and FAC5. The EDX spectra of both FA5 and FAC5 materials revealed the presence of O, Fe, and Ag peaks. In addition, the EDX spectrum of FAC5 shows a prominent signal peak at 0.27 keV, which is characteristic of the C element of CNC in the material.
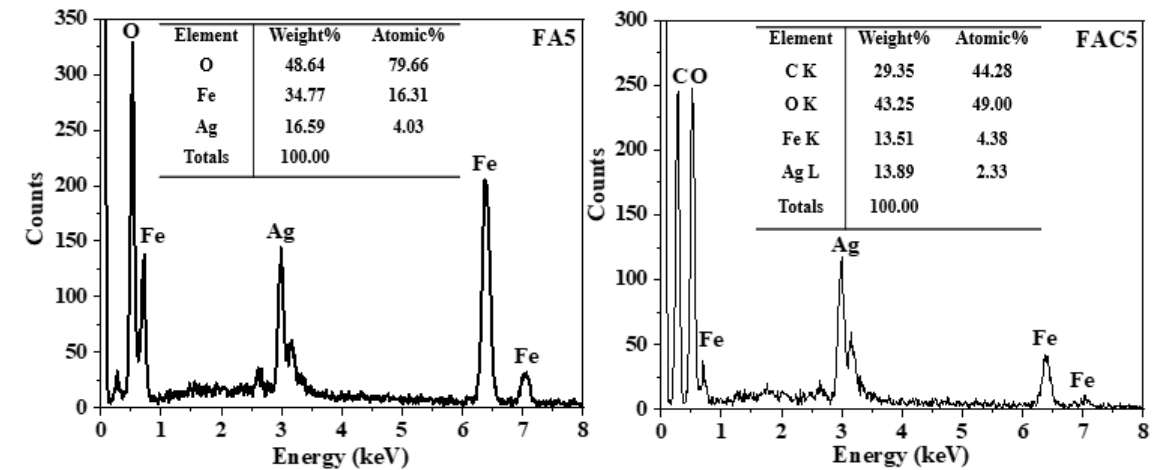

Figure 6. EDX spectra of FA5 and FAC5**.**

The magnetic property of our materials was investigated using a vibrating sample magnetometer (VSM). All of our magnetic hysteresis is depicted in Figure 7. The saturation magnetization (M_s), remanent magnetization (M_r), and coercivity (H_c) values of seven samples are displayed in Table 1 based on the results of the VSM, from Fe_3O_4 to FA to FAC, the Ms of the samples decreased. The saturation of magnetization of Fe_3O_4 reduces when Ag nanoparticles are present on the Fe_3O_4 surface and reduces more when having CNC. This result is consistent with previous research [40–42].
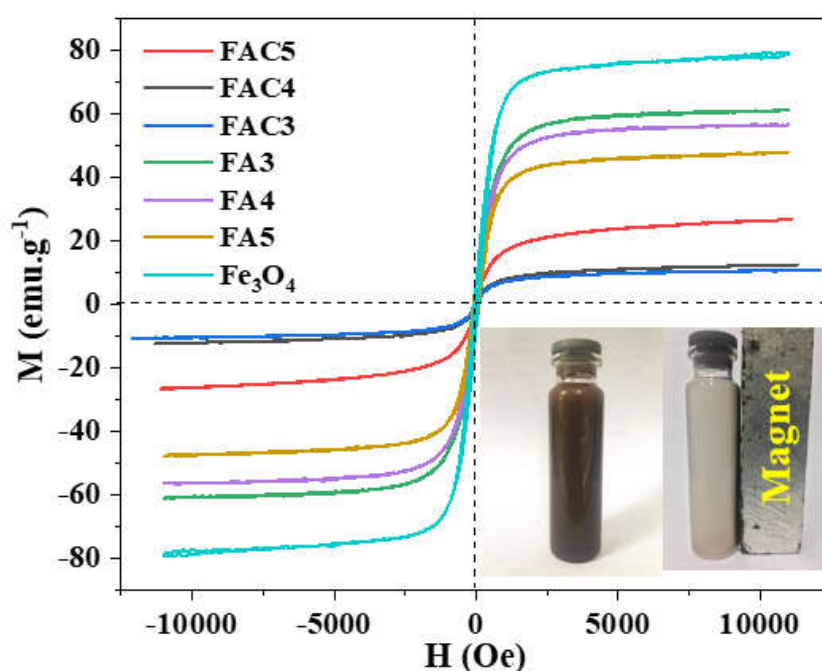
Figure 7. M-H loops of Fe_3O_4, FA, and FAC materials.

Table 1. The M_s, M_r, and H_c values of seven samples.

No.	Sample	M_s (emu/g)	M_r (emu/g)	H_c (Oe)
1	Fe_3O_4	78.5	6.5	61.6
2	FA3	61.1	7.7	102.6
3	FA4	56.4	5.9	75.2
4	FA5	47.7	5.9	82.1
5	FAC3	10.6	0.1	6.8
6	FAC4	12.4	0.2	15.9
7	FAC5	26.6	0.4	6.8

In contrast to FA materials, the Ms value of FAC materials increases with increasing hydrothermal duration in the presence of CNC. The phase composition of the materials may cause this result. As mentioned in the XRD results, FAC3 and FAC4 samples have low M_s due to impurity phases with diffraction peaks at $2\theta = 27.7^o$ and 32.1^o. These peaks disappeared in the FAC5 sample after 5 hours of hydrothermal treatment, so FAC5 has a higher Ms than FAC3 and FAC4 samples. Even though the magnetism of FAC5 is significantly diminished compared to that of pure Fe_3O_4, it can be readily separated from the solution by applying an external magnetic field (Figure 7). This magnetic behavior not only makes the FAC5 catalyst economically viable for recovery and reuse, but it also precludes the production of secondary sources of pollution, which are generated by catalyst residues that are not recovered after processing.

Figure 8 depicts the TGA and DTG of CNC and FAC5. According to Alvarez and Va1zquez, the decomposition temperature of cellulose is approximately 360 °C, where high-weight macromolecules are broken down into small-weight glucose units [43]. The DTG curves (Figure 8b) reveal that CNC has the highest decomposition temperature at 357.0 °C, and the initial decomposition temperature is relatively high at 315.0 °C. Upon hydrolysis by HCl acid, hydroxyl groups on the cellulose surface tend to interact to form densely packed hydrogen bonding networks around nano cellulose, resulting in a higher decomposition temperature [44].

The TGA results (Figure 8a) indicate that after Ag and Fe_3O_4 are bonded to the CNC template, the material decomposes at approximately 284.0 °C and reaches its maximal temperature of 297.1 °C.

It can explain that when metal and metal oxide form on the CNC surface, the metal decomposes faster than the initial CNC due to its high heat conductivity. In addition, a significant amount of FAC5 decomposes at 343 °C, with the highest decomposition temperature occurring at 364.6 °C. It is the thermal degradation region of cellulose, where the weight loss is relatively high, and the charred residue exceeds the initial CNC (13.7%). According to FAC5, metals, and metal oxides have high heat resistance, and they remain in the structure after cellulose decomposes completely, resulting in the sample's thermal stability. Therefore, FAC5 has a reduced decomposition rate and more char residue than CNC.
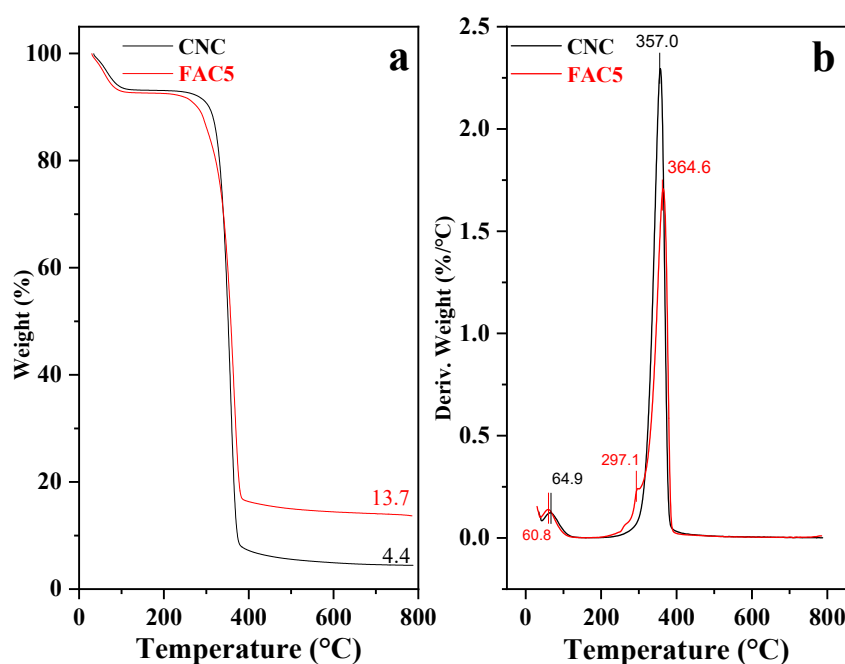

Figure 8. TGA (a) and DTG (b) curves of CNC and FAC5.

3.2. Catalytic Reduction of 4-NP

The reduction of 4-NP in excess $NaBH_4$ was selected as a model reaction to evaluate the catalytic activity of the prepared FAC5 nanocomposite. UV–vis absorption spectroscopy was used to track the progression of the catalytic reduction. During the experiment, the peak UV absorption of an aqueous solution of 4-NP moved with increasing intensity from 318 to 400 nm after adding freshly generated $NaBH_4$ solution. The production of 4-nitrophenolate ions with a more vital -conjugated donor-acceptor characteristic is probably responsible for the initial color change (mild to intense yellow) followed by a red shift when $NaBH_4$ solution is added [45]. After a delay, the UV absorption peak of 4-NP at 400 nm and its brilliant yellow color disappeared upon adding the FAC5 catalyst. The development and progressive strengthening of a new peak at 300 nm confirms the progression of the reaction due to the production of 4-AP. Figure 9 depicts the absorption spectrum of 4-NP as a function of time for the catalysts FA5 and FAC5. In the presence of 2.5 mg FAC5, 4-NP was nearly completely reduced within 10 min, accompanied by a change in color from vibrant yellow to colorless. C_t and C_0 were the absorbance values of 4-NP in the presence of $NaBH_4$ at time $t = t$ and $t = 0$, respectively, and were plotted against time (t) in Figure 9 in the presence of the FA5 and FAC5 catalysts. FAC5 has higher catalytic activity than FA5. After 60 min, the absorption peak of 4-NP at 400 nm in $NaBH_4$ and without the catalyst is almost unchanged.

Similarly, 4-NP reduction proceeded very slowly when it occurred in the presence of a catalyst but without $NaBH_4$ as a reducer. These occurrences indicate that the reaction requires both the catalyst and reducing agent ($NaBH_4$). In addition, the potential catalytic activity of the CNC and Fe_3O_4 adsorbent was examined in the presence and absence of $NaBH_4$ under conditions analogous to those

stated for FAC5. After 60 min of reaction, however, the absorption peak intensity at 400 nm kept unchanged relative to that of the initial 4-NP, indicating that Ag NPs played a crucial role in the conversion of -NO$_2$.
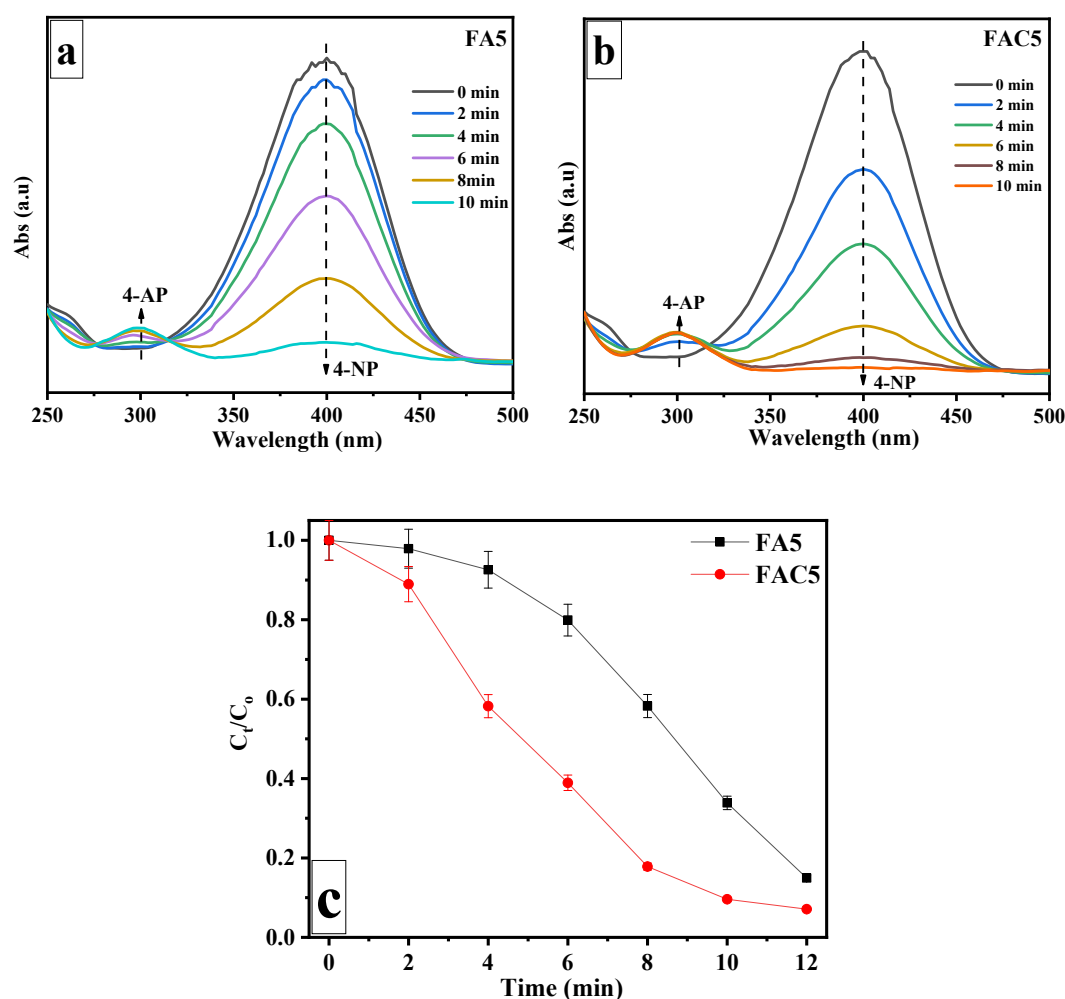

Figure 9. Changes in UV–vis absorption spectra for the reduction of 4-NP by NaBH$_4$ over time in the presence of (a) FA5 and (b) FAC5 catalysts; (c) the corresponding plot of (C_t/C_o) versus reaction time (t).

3.3. Removal of MO and MB via Adsorption Process and Catalytic Reduction

At ambient temperature, the adsorption of two water-soluble organic dyes (MB and MO) was tested using CNC, FA5, and FAC5. 15.0 mg of each substance was added to a 30 mL beaker containing a 1.0×10^{-4} M aqueous dye solution. The mixture was agitated at 300 rounds per min. The experiments were evaluated by measuring the absorbance of the dye solution at intervals and then determining the MB concentration using the dye calibration curve. The dye removal was calculated using the following formula:

$$\text{Dye removal} = \frac{C_t}{C_o} \times 100 \qquad (1)$$

where C_t is the dye concentration at time t, and C_o is the initial dye concentration.

Figure 10a,c depict the (C_t/C_0) versus time profiles for determining the remaining MB and MO after using CNC, FA5, and FAC5 adsorbents. All materials generally possess MB adsorption, and the equivalence is reached in 10 min. Due to the electrostatic interaction between the negatively charged hydroxyl groups on the surface of CNC and the positively charged cation MB dye, CNC exhibits excellent MB adsorption. Twenty-five percent of MB remained after a 30-minute test on CNC. FA5's

adsorption MB is significantly lower than that of CNC. After 30 min of MB adsorption, the remaining MB concentration in FA5 was 48.3%. Upon the appearance of Ag/Fe_3O_4 on the CNC surface, the MB dye's absorption increased dramatically compared to Ag/Fe_3O_4. The FAC5 material exhibited the highest adsorption efficacy, as shown in Figure 10a. After 30 min, the remaining concentration of MB was 10.5%. The presence of CNC in the hydrothermal process facilitates the uniform dispersion of Ag/Fe_3O_4 on the CNC surface, increasing the surface area of FAC5 relative to FA5. The results shown in Figure 11a provide information regarding the two samples' BET surface area (S_{BET}). According to the International Union of Pure and Applied Chemistry (IUPAC) classification, the evaluated materials exhibited type IV patterns with hysteresis loops. Two samples exhibited narrow H3-type hysteresis loops (parallel plate-shaped apertures) based on the hysteresis loop patterns. In addition, the zeta potential values of the FAC5 suspension obtained through DLS analysis were -27.2 ± 1.1 mV negative (Figure 11b). This also facilitates enhanced cationic MB dye adsorption. MO, as opposed to MB, is a negative anion dye. Thus, CNC hardly absorbs MO. FA5 and FAC5 adsorption on MO also occurred and reached equilibrium after 10 min of agitating both substances in the MO solution. Due to its greater surface area, FAC5 has a higher MO adsorption capacity than FA5.
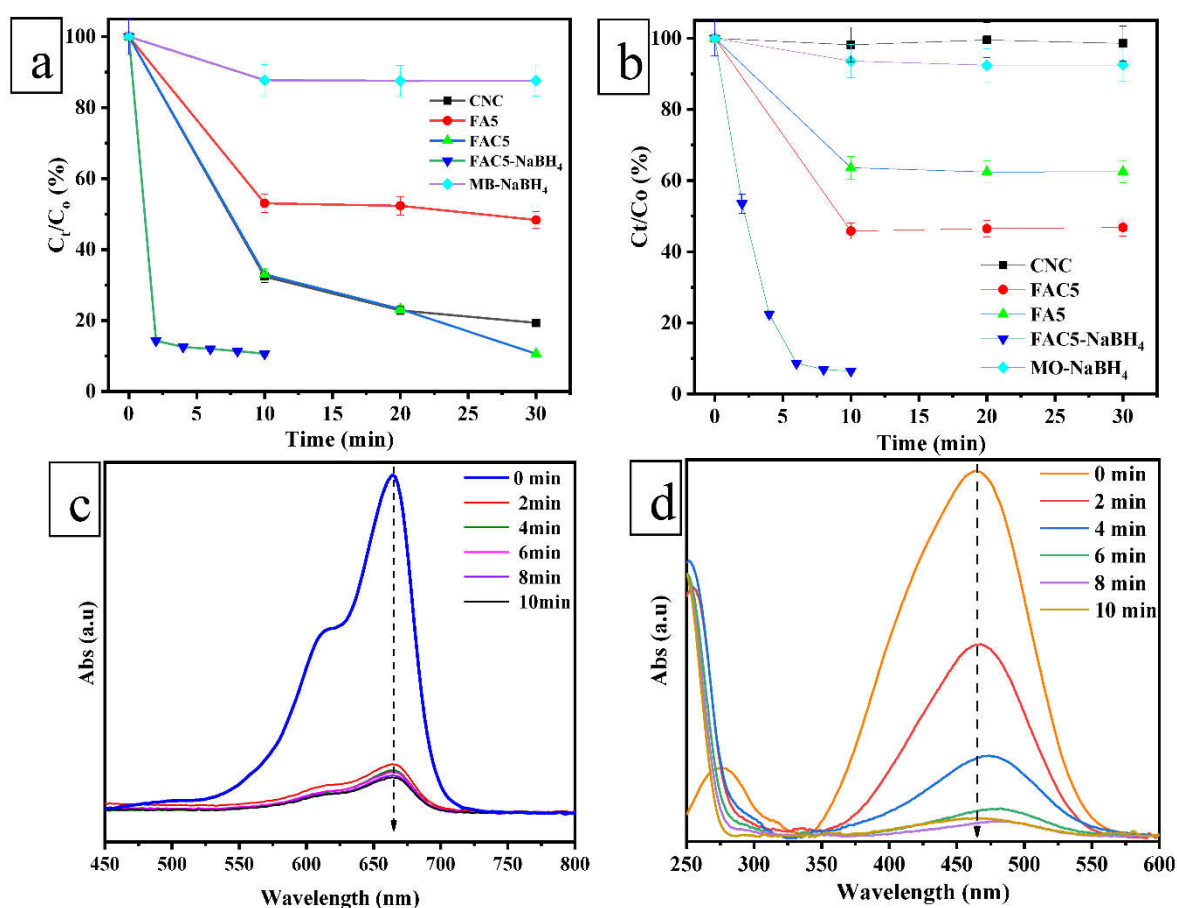

Figure 10. The graph of (C_t/C_o) vs. time (t) for (a) MB and (c) MO; UV–vis absorption spectrum changes for the reduction of (b) MB and (d) MO by $NaBH_4$ at different time intervals in the presence of FAC5 catalyst.
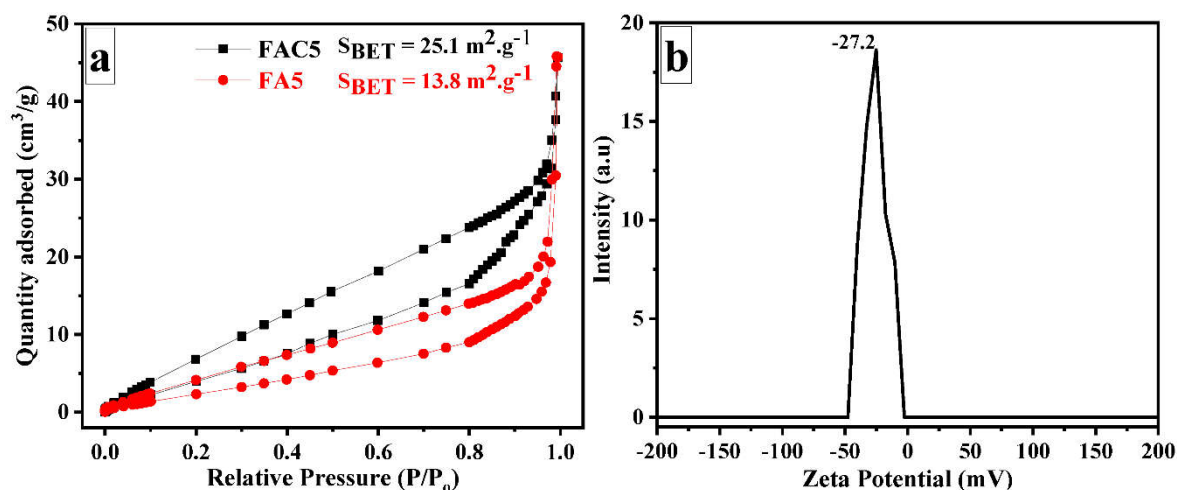
Figure 11. (a) Nitrogen adsorption and desorption isotherms of FA5 and FAC5 materials; (b) zeta potential distribution of FAC5 material.
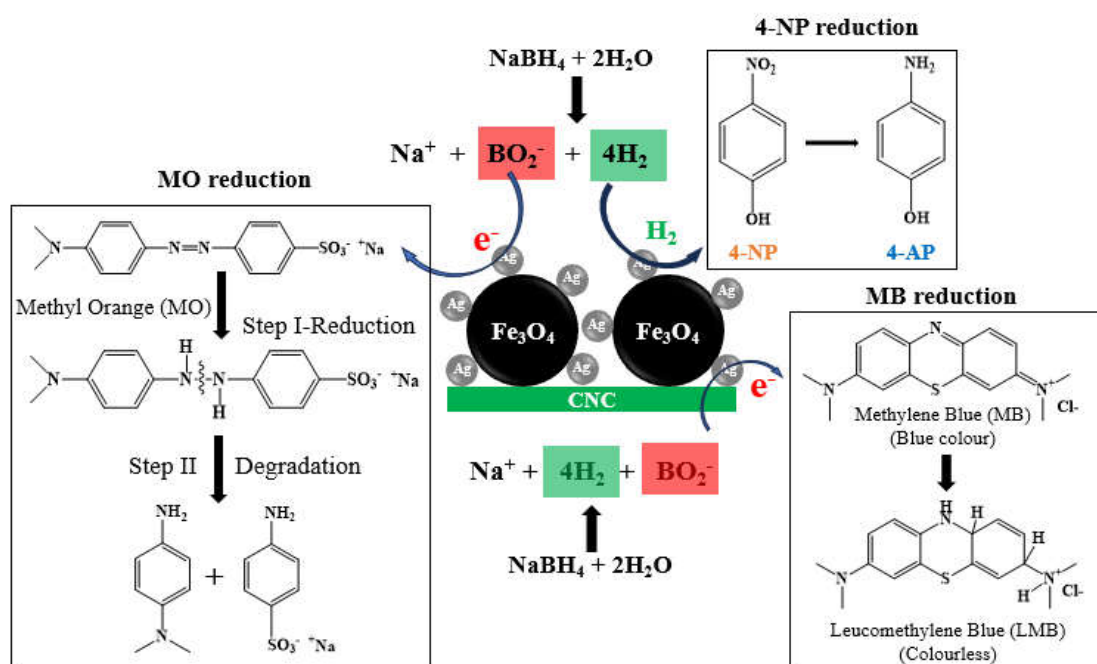

Figure 12. A possible way for 4-NP and organic dyes (MO and MB) to be broken down by FAC5 nanocomposite.

Given the outstanding adsorption behavior of FAC5 nanocomposite for MB, our next objective was to investigate its performance in degrading hazardous organic dyes using $NaBH_4$ as a reducing agent and monitoring the variation in the intensity of the UV absorption peak at λ_{max} = 664 nm [46,47] allowed for the evaluation of the MB catalytic degradation process. Figure 10b also depicts the time-dependent change in the modification in the MB absorption spectrum. Within 10 min, the MB dye solution completely lost its color, from the intense blue color (MB) to colorless leucomethylene blue (LMB). In addition, the reduction of MO was comparable to that of MB. Figure 10d depicts the UV–vis absorption maximum variation at λ_{max} = 464 nm for MO [48,49] at various time intervals. As the reduction progressed, it was observed that the characteristic peak intensity decreased significantly

and nearly disappeared within 10 min. There was no significant change in the distinct absorption peak of MB and MO after 60 min of exposure without a catalyst or a reductant.

Figure 12 depicts a potential mechanism for reducing 4-NP and organic dyes using the FAC5 catalyst with $NaBH_4$ based on the above experimental results. In addition, the experimental results indicate that the reduction rate is significantly accelerated in the presence of Ag metal on the catalyst's surface compared to $NaBH_4$ alone. Figure 12 shows that hydrolysis of borohydride ions in aqueous solution generates H_2 gas and BO_2^- [50–52]. As the hydrogen mediator for the reduction of 4-NP, 4-NP is deposited onto the surface of Ag NPs to produce a silver hydride complex. Ag NPs serve as redox catalysts for dye reduction by conveying electrons between donor species (BO_2^-) and acceptor molecules (MO or MB) [53–56]. The MB experiment observed that the colorless (reduced) form of MB (LMB) underwent sluggish aerial oxidation in an open atmosphere after 3–4 hours. However, the characteristic blue color dissipated upon shacking, as the excess $NaBH_4$ in solution once again diminished it. Similar observations, called "clock" reactions, have been reported in the past [57]. In contrast, the reduced MO solution did not change color even after several days, indicating no subsequent re-oxidation. As shown in Figure 12, the MO decolorization products were N, N-dimethyl-benzene-1,4-diamine, and 4-aminobenzenesulfonate, formed via hydrogenation and subsequent -NH-NH- bond dissociation [58].
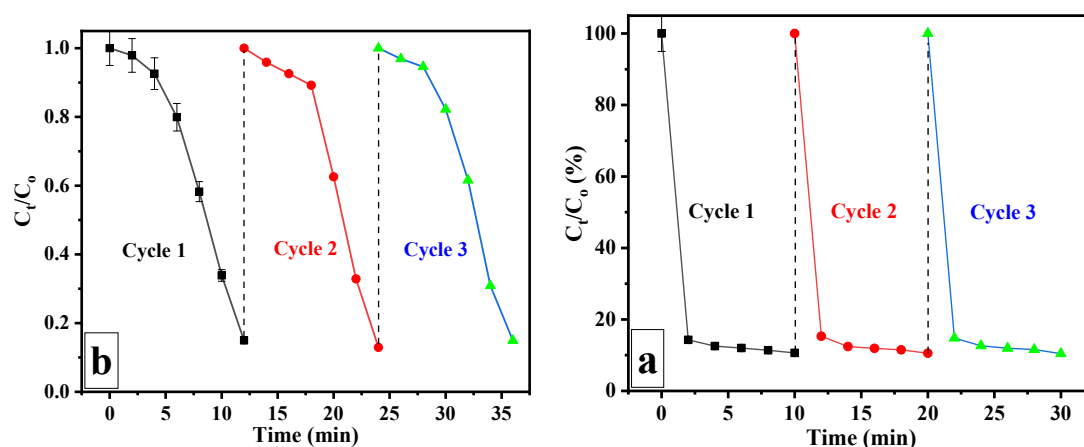

Figure 13. Reusability of FAC5 catalyst over three successive cycles for reduction of (a) MB and (b) 4-NP.

The recyclability of FAC5 nanocomposite was an essential factor for more cost-effective processes, and we examined the sample's efficiency in repeated reaction cycles. The FAC5 nanocomposite could be readily separated from the solution by an external magnetic field due to its strong magnetic properties. The nanocomposite was utilized for the MB and 4-NP reduction after being washed five times with distilled water. After three repetitions of this procedure, the FAC5 nanocomposite remained stable and exhibited a high level of reactive activity, indicating its outstanding recyclability. As depicted in Figure 13, the FAC5 was effectively reused in three successive 10-minute cycles. It was observed that the catalyst had not significantly lost activity after three cycles. This result indicates that the FAC5 nanocomposite developed in the present study is exceptionally stable and resistant to multiple reuse cycles.

4. Conclusions

Using a straightforward protocol, a magnetic CNC nanocomposite decorated with Ag NPs ($Ag/Fe_3O_4/CNC$) was synthesized at ambient temperature without adding any reducing agent or stabilizer. In this green synthesis method, the CNC matrix was essential for reducing the Ag^+ precursor and stabilizing newly formed Ag NPs on its surface. On the CNC surface, XRD and EDX analyses have confirmed the formation of Ag NPs. TEM and FE-SEM investigations also confirmed that the magnetic nanocomposite's surface was decorated with Ag NPs, and in the presence of

$NaBH_4$, the $Ag/Fe_3O_4/CNC$ nanocomposite exhibited exceptional catalytic activity for reducing 4-NP to 4-AP. It appeared to be an impressive catalyst for the rapid reduction and decolorization of toxic organic substances (both MB and MO) in a few min (2.0–5.0) with a tiny amount of catalyst (2.5 mg for 4-NP and 15 mg for MB and MO). Hydrolysis of borohydride ions in aqueous solution resulted in the formation of H_2 gas and electron-rich BO_2^- ions as intermediates for the construction of a hydrogen-mediator complex (silver hydride) and an electron relay system for the reduction of organic species (4-NP, MO, and MB). Therefore, $Ag/Fe_3O_4/CNC$ is a potentially helpful catalyst for removing organic toxic pollutants from contaminated water bodies.

Author Contributions: V.N.A.: Formal analysis, Investigation, Writing—Original Draft Preparation, L.T.N.H.: Investigation, Writing—Review & Editing, P.B.T.: Investigation, and L.V.H.: Conceptualization, Methodology, Supervision. All authors have read and agreed to the published version of the manuscript.

Data Availability Statement: The data presented in this study are available in this published article.

Conflicts of Interest: The authors declare that they have no known competing financial interests or personal relationships that could have appeared to influence the work reported in this paper.

References

1. Zhang, H.; Chen, D.; Lv, X.; Wang, Y.; Chang, H.; Li, J., Energy-Efficient Photodegradation of Azo Dyes with TiO2 Nanoparticles Based on Photoisomerization and Alternate UV–Visible Light. *Environ. Sci. Technol.* **2010**, *44*, 1107–1111.
2. Mou, F.; Guan, J.; Ma, H.; Xu, L.; Shi, W., Magnetic Iron Oxide Chestnutlike Hierarchical Nanostructures: Preparation and Their Excellent Arsenic Removal Capabilities. *ACS Appl. Mater. Interfaces* **2012**, *4*, 3987–3993.
3. Ma, Y.; Wu, X.; Zhang, G., Core-shell Ag@Pt nanoparticles supported on sepiolite nanofibers for the catalytic reduction of nitrophenols in water: Enhanced catalytic performance and DFT study. *Appl. Catal. B: Environ.* **2017**, *205*, 262–270.
4. Hai, F.I.; Yamamoto, K.; Fukushi, K., Hybrid Treatment Systems for Dye Wastewater. *Crit. Rev. Environ. Sci. Technol.* **2007**, *37*, 315–377.
5. Martínez-Huitle, C.A.; Brillas, E., Decontamination of wastewaters containing synthetic organic dyes by electrochemical methods: A general review. *Appl. Catal. B: Environ.* **2009**, *87*, 105–145.
6. Gupta, A.K.; Pal, A.; Sahoo, C., Photocatalytic degradation of a mixture of Crystal Violet (Basic Violet 3) and Methyl Red dye in aqueous suspensions using Ag+ doped TiO2. *Dye. Pigment.* **2006**, *69*, 224–232.
7. Yang, J.; Pan, B.; Li, H.; Liao, S.; Zhang, D.; Wu, M.; Xing, B., Degradation of p-Nitrophenol on Biochars: Role of Persistent Free Radicals. *Environ. Sci. Technol.* **2016**, *50*, 694–700.
8. Yi, S.; Zhuang, W.-Q.; Wu, B.; Tay, S.T.-L.; Tay, J.-H., Biodegradation of p-Nitrophenol by Aerobic Granules in a Sequencing Batch Reactor. *Environ. Sci. Technol.* **2006**, *40*, 2396–2401.
9. Shen, J.; Xu, X.; Jiang, X.; Hua, C.; Zhang, L.; Sun, X.; Li, J.; Mu, Y.; Wang, L., Coupling of a bioelectrochemical system for p-nitrophenol removal in an upflow anaerobic sludge blanket reactor. *Water Res.* **2014**, *67*, 11–18.
10. Deka, P.; Deka, R.C.; Bharali, P., In situ generated copper nanoparticle catalyzed reduction of 4-nitrophenol. *New J. Chem.* **2014**, *38*, 1789–1793.
11. Liu, H.; Bi, Z.; Sun, X.-G.; Unocic, R.R.; Paranthaman, M.P.; Dai, S.; Brown, G.M., Mesoporous TiO2–B Microspheres with Superior Rate Performance for Lithium Ion Batteries. *Adv. Mater.* **2011**, *23*, 3450–3454.
12. Chang, J.; Sun, J.; Xu, C.; Xu, H.; Gao, L., Template-free approach to synthesize hierarchical porous nickel cobalt oxides for supercapacitors. *Nanoscale* **2012**, *4*, 6786–6791.
13. He, K.; Chen, G.; Zeng, G.; Chen, A.; Huang, Z.; Shi, J.; Huang, T.; Peng, M.; Hu, L., Three-dimensional graphene supported catalysts for organic dyes degradation. *Appl. Catal. B: Environ.* **2018**, *228*, 19–28.
14. Astruc, D.; Lu, F.; Aranzaes, J.R., Nanoparticles as Recyclable Catalysts: The Frontier between Homogeneous and Heterogeneous Catalysis. *Angew. Chem. Int. Ed.* **2005**, *44*, 7852–7872.
15. Ji, T.; Chen, L.; Schmitz, M.; Bao, F.S.; Zhu, J., Hierarchical macrotube/mesopore carbon decorated with mono-dispersed Ag nanoparticles as a highly active catalyst. *Green Chem.* **2015**, *17*, 2515–2523.
16. Huang, Z.; Zeng, Z.; Chen, A.; Zeng, G.; Xiao, R.; Xu, P.; He, K.; Song, Z.; Hu, L.; Peng, M.; Huang, T.; Chen, G., Differential behaviors of silver nanoparticles and silver ions towards cysteine: Bioremediation and toxicity to Phanerochaete chrysosporium. *Chemosphere* **2018**, *203*, 199–208.

17. He, J.; Ji, W.; Yao, L.; Wang, Y.; Khezri, B.; Webster, R.D.; Chen, H., Strategy for Nano-Catalysis in a Fixed-Bed System. *Adv. Mater.* **2014**, *26*, 4151–4155.

18. Dai, Y.; Zheng, W.; Li, X.; Chen, B.; Wang, L.; He, G., Highly active catalysis–membrane system: Enhanced recyclability, durability and longevity properties for H2 generation. *Chem. Eng. J.* **2016**, *293*, 252–258.

19. Warner, C.L.; Addleman, R.S.; Cinson, A.D.; Droubay, T.C.; Engelhard, M.H.; Nash, M.A.; Yantasee, W.; Warner, M.G., High-Performance, Superparamagnetic, nanoparticle-based heavy metal sorbents for removal of contaminants from natural waters. *ChemSusChem* **2010**, *3*, 749–757.

20. Liu, Y.; Chen, J.-F.; Bao, J.; Zhang, Y., Manganese-Modified Fe3O4 Microsphere Catalyst with Effective Active Phase of Forming Light Olefins from Syngas. *ACS Catal.* **2015**, *5*, 3905–3909.

21. Das, R.; Sypu, V.S.; Paumo, H.K.; Bhaumik, M.; Maharaj, V.; Maity, A., Silver decorated magnetic nanocomposite (Fe3O4@ PPy-MAA/Ag) as highly active catalyst towards reduction of 4-nitrophenol and toxic organic dyes. *Appl. Catal. B: Environ.* **2019**, *244*, 546–558.

22. Liu, Y.; Zhang, Y.; Kou, Q.; Wang, D.; Han, D.; Lu, Z.; Chen, Y.; Chen, L.; Wang, Y.; Zhang, Y., Fe3O4/Au binary nanocrystals: Facile synthesis with diverse structure evolution and highly efficient catalytic reduction with cyclability characteristics in 4-nitrophenol. *Powder Technol.* **2018**, *338*, 26–35.

23. Yılmaz Baran, N.; Baran, T.; Menteş, A., Production of novel palladium nanocatalyst stabilized with sustainable chitosan/cellulose composite and its catalytic performance in Suzuki-Miyaura coupling reactions. *Carbohydr Polym* **2018**, *181*, 596–604.

24. Wang, G.; Chen, Y.; Xu, G.; Pei, Y., Effective removing of methylene blue from aqueous solution by tannins immobilized on cellulose microfibers. *Int J Biol Macromol* **2019**, *129*, 198–206.

25. Ibnu Abdulwahab, M.; Khamkeaw, A.; Jongsomjit, B.; Phisalaphong, M., Bacterial Cellulose Supported Alumina Catalyst for Ethanol Dehydration. *Catal. Lett.* **2017**, *147*, 2462–2472.

26. Rodrigues, D.M.; Hunter, L.G.; Bernard, F.L.; Rojas, M.F.; Vecchia, F.D.; Einloft, S., Harnessing CO2 into Carbonates Using Heterogeneous Waste Derivative Cellulose-Based Poly(ionic liquids) as Catalysts. *Catal. Lett.* **2018**, *149*, 733–743.

27. Peng, S.; Gao, F.; Zeng, D.; Peng, C.; Chen, Y.; Li, M., Synthesis of Ag–Fe3O4 nanoparticles supported on polydopamine-functionalized porous cellulose acetate microspheres: catalytic and antibacterial applications. *Cellulose* **2018**, *25*, 4771–4782.

28. Guo, L.; Duan, B.; Zhang, L., Construction of controllable size silver nanoparticles immobilized on nanofibers of chitin microspheres via green pathway. *Nano Res.* **2016**, *9*, 2149–2161.

29. Maleki, A.; Movahed, H.; Ravaghi, P., Magnetic cellulose/Ag as a novel eco-friendly nanobiocomposite to catalyze synthesis of chromene-linked nicotinonitriles. *Carbohydr. Polym.* **2016,** *156*.

30. Shojaei, S.; Ghasemi, Z.; Shahrisa, A., Cu(I)@Fe3O4 nanoparticles supported on imidazolium-based ionic liquid-grafted cellulose: Green and efficient nanocatalyst for multicomponent synthesis of N-sulfonylamidines and N-sulfonylacrylamidines. *Appl. Organomet. Chem.* **2017**, *31*, e3788.

31. Pei, Y.; Zhao, J.; Shi, R.; Wang, X.; Li, Z.; Ren, J., Hierarchical Porous Carbon-Supported Copper Nanoparticles as an Efficient Catalyst for the Dimethyl Carbonate Synthesis. *Catal. Lett.* **2019**, *149*, 3184–3193.

32. Karami, S.; Zeynizadeh, B.; Shokri, Z., Cellulose supported bimetallic F… Cu nanoparticles: a magnetically recoverable nanocatalyst for quick reduction of nitroarenes to amines in water. *Cellulose* **2018**, *25*, 3295–3305.

33. Cai, J.; Liu, Y.; Zhang, L., Dilute solution properties of cellulose in LiOH/urea aqueous system. *J. Polym. Sci. Part B: Polym. Phys.* **2006**, *44*, 3093–3101.

34. Wang, G., Selective hydrothermal degradation of cellulose to formic acid in alkaline solutions. *Cellulose* **2018,** *v. 25* (no. 10), pp. 5659–5668-2018 v.25 no.10.

35. Luo, X.; Liu, S.; Zhou, J.; Zhang, L., In situ synthesis of Fe3O4/cellulose microspheres with magnetic-induced protein delivery. *J. Mater. Chem.* **2009**, *19*, 3538–3545.

36. Nang An, V.; Chi Nhan, H.T.; Tap, T.D.; Van, T.T. T.; Van Viet, P.; Van Hieu, L., Extraction of High Crystalline Nanocellulose from Biorenewable Sources of Vietnamese Agricultural Wastes. *J. Polym. Environ.* **2020**, *28*, 1465–1474.

37. Xing, Y.; Jin, Y.-Y.; Si, J.-C.; Peng, M.-L.; Wang, X.-F.; Chen, C.; Cui, Y.-L., Controllable synthesis and characterization of Fe3O4/Au composite nanoparticles. *J. Magn. Magn. Mater.* **2015**, *380*, 150–156.

38. Xing, Y.; Gao, Q.; Zhang, Y.; Ma, L.; Loh, K.Y.; Peng, M.; Chen, C.; Cui, Y., The improved sensitive detection of C-reactive protein based on the chemiluminescence immunoassay by employing monodispersed PAA-Au/Fe3O4 nanoparticles and zwitterionic glycerophosphoryl choline. *J. Mater. Chem. B* **2017**, *5*, 3919–3926.

39. Xiong, R.; Lu, C.; Wang, Y.; Zhou, Z.; Zhang, X., Nanofibrillated cellulose as the support and reductant for the facile synthesis of Fe 3 O 4/Ag nanocomposites with catalytic and antibacterial activity. *J. Mater. Chem. A* **2013**, *1*, 14910–14918.

40. Khan, F.S. A.; Mubarak, N.M.; Khalid, M.; Walvekar, R.; Abdullah, E.C.; Mazari, S.A.; Nizamuddin, S.; Karri, R.R., Magnetic nanoadsorbents' potential route for heavy metals removal—a review. *Environ. Sci. Pollut. Res.* **2020**, *27*, 24342–24356.

41. Wang, G.; Li, F.; Li, L.; Zhao, J.; Ruan, X.; Ding, W.; Cai, J.; Lu, A.; Pei, Y., In Situ Synthesis of Ag–Fe3O4 Nanoparticles Immobilized on Pure Cellulose Microspheres as Recyclable and Biodegradable Catalysts. *ACS Omega* **2020**, *5*, 8839–8846.

42. Babu, A.T.; Sebastian, M.; Manaf, O.; Antony, R., Heterostructured Nanocomposites of Ag Doped Fe3O4 Embedded in ZnO for Antibacterial Applications and Catalytic Conversion of Hazardous Wastes. *J. Inorg. Organomet. Polym. Mater.* **2019**.

43. Alvarez, V.A.; Vázquez, A., Thermal degradation of cellulose derivatives/starch blends and sisal fibre biocomposites. *Polym. Degrad. Stab.* **2004**, *84*, 13–21.

44. Kargarzadeh, H.; Ishak, b.; Ahmad, I.; Abdullah, I.; Dufresne, A.; Siti, b.; Zainudin, Y.; Rasha, b.; Sheltami, M., Effects of hydrolysis conditions on the morphology, crystallinity, and thermal stability of cellulose nanocrystals extracted from kenaf bast fibers. *Cellulose* **2012**, *19*, 855–866.

45. Choi, Y.; Bae, H.S.; Seo, E.; Jang, S.; Park, K.H.; Kim, B.-S., Hybrid gold nanoparticle-reduced graphene oxide nanosheets as active catalysts for highly efficient reduction of nitroarenes. *J. Mater. Chem.* **2011**, *21*, 15431–15436.

46. Veerakumar, P.; Chen, S.-M.; Madhu, R.; Veeramani, V.; Hung, C.-T.; Liu, S.-B., Nickel Nanoparticle-Decorated Porous Carbons for Highly Active Catalytic Reduction of Organic Dyes and Sensitive Detection of Hg(II) Ions. *ACS Appl. Mater. Interfaces* **2015**, *7*, 24810–24821.

47. Mignani, A.; Fazzini, S.; Ballarin, B.; Boanini, E.; Cassani, M.C.; Maccato, C.; Barreca, D.; Nanni, D., Mild fabrication of silica-silver nanocomposites as active platforms for environmental remediation. *RSC Adv.* **2015**, *5*, 9600–9606.

48. Hu, B.; Zhao, Y.; Zhu, H.-Z.; Yu, S.-H., Selective Chromogenic Detection of Thiol-Containing Biomolecules Using Carbonaceous Nanospheres Loaded with Silver Nanoparticles as Carrier. *ACS Nano* **2011**, *5*, 3166–3171.

49. Rajesh, R.; Kumar, S.S.; Venkatesan, R., Efficient degradation of azo dyes using Ag and Au nanoparticles stabilized on graphene oxide functionalized with PAMAM dendrimers. *New J. Chem.* **2014**, *38*, 1551–1558.

50. Carregal-Romero, S.; Pérez-Juste, J.; Hervés, P.; Liz-Marzán, L.M.; Mulvaney, P., Colloidal Gold-Catalyzed Reduction of Ferrocyanate (III) by Borohydride Ions: A Model System for Redox Catalysis. *Langmuir* **2010**, *26*, 1271–1277.

51. Chishti, A.N.; Ma, Z.; Zha, J.; Ahmad, M.; Wang, P.; Gautam, J.; Chen, M.; Ni, L.; Diao, G., Preparation of novel magnetic noble metals supramolecular composite for the reduction of organic dyes and nitro aromatics. *Chin. Chem. Lett.* **2023**, *34*, 108122.

52. Singh, S.; Sharma, S.; Manhas, U.; Qadir, I.; Atri, A.K.; Singh, D., Different Fuel-Adopted Combustion Syntheses of Nano-Structured NiCrFeO4: A Highly Recyclable and Versatile Catalyst for Reduction of Nitroarenes at Room Temperature and Photocatalytic Degradation of Various Organic Dyes in Unitary and Ternary Solutions. *ACS Omega* **2022**, *7*, 19853–19871.

53. Mallick, K.; Witcomb, M.; Scurrell, M., Silver nanoparticle catalysed redox reaction: An electron relay effect. *Mater. Chem. Phys.* **2006**, *97*, 283–287.

54. Nautiyal, A.; Shukla, S.R., Silver nanoparticles catalyzed reductive decolorization of spent dye bath containing acid dye and its reuse in dyeing. *J. Water Process Eng.* **2018**, *22*, 276–285.

55. He, L.; Zhou, Z.; Liu, Z.; Nan, X.; Wang, T.; Sun, X.; Bai, P., Morphology design and synthesis of magnetic microspheres as highly efficient reusable catalyst for organic dyes. *Colloids Surf. A: Physicochem. Eng. Asp.* **2023**, *656*, 130542.

56. Hunge, Y.M.; Yadav, A.A.; Kang, S.-W.; Kim, H., Facile synthesis of multitasking composite of Silver nanoparticle with Zinc oxide for 4-nitrophenol reduction, photocatalytic hydrogen production, and 4-chlorophenol degradation. *J. Alloys Compd.* **2022**, *928*, 167133.

57. Pande, S.; Jana, S.; Basu, S.; Sinha, A.K.; Datta, A.; Pal, T., Nanoparticle-Catalyzed Clock Reaction. *J. Phys. Chem. C* **2008**, *112*, 3619–3626.

58. Jia, Z.; Sun, H.; Du, Z.; Lei, Z., Catalytic bubble-free hydrogenation reduction of azo dye by porous membranes loaded with palladium nanoparticles. *J. Environ. Sci.* **2014**, *26*, 478–482.